Enhancing crystal integrity and structural rigidity of $CsPbBr_3$ nanoplatelets to achieve a narrow color-saturated blue emission

Huang, Qianqian; Yin, Wenxu; Gao, Bo; Zeng, Qingsen; Yao, Dong; Zhang, Hao; Zhao, Yinghe; Zheng, Weijia; Zhang, Jiaqi; Yang, Xuyong; Zhang, Xiaoyu; Rogach, Andrey L.

Published in:
Light: Science and Applications

Published: 01/01/2024

Document Version:
Final Published version, also known as Publisher's PDF, Publisher's Final version or Version of Record

Published version (DOI):
10.1038/s41377-024-01441-1

Publication details:
Huang, Q., Yin, W., Gao, B., Zeng, Q., Yao, D., Zhang, H., Zhao, Y., Zheng, W., Zhang, J., Yang, X., Zhang, X., & Rogach, A. L. (2024). Enhancing crystal integrity and structural rigidity of $CsPbBr_3$ nanoplatelets to achieve a narrow color-saturated blue emission. *Light: Science and Applications*, *13*(1), Article 111. https://doi.org/10.1038/s41377-024-01441-1

Official journal of the CIOMP 2047-7538
www.nature.com/lsa

ARTICLE Open Access

Enhancing crystal integrity and structural rigidity of $CsPbBr_3$ nanoplatelets to achieve a narrow color-saturated blue emission

Qianqian Huang[1], Wenxu Yin[1], Bo Gao[1], Qingsen Zeng[2], Dong Yao[2], Hao Zhang[2], Yinghe Zhao[3], Weijia Zheng[4]✉, Jiaqi Zhang[1], Xuyong Yang[5], Xiaoyu Zhang[1]✉ and Andrey L. Rogach[6]✉

Abstract

Quantum-confined $CsPbBr_3$ perovskites are promising blue emitters for ultra-high-definition displays, but their soft lattice caused by highly ionic nature has a limited stability. Here, we endow $CsPbBr_3$ nanoplatelets (NPLs) with atomic crystal-like structural rigidity through proper surface engineering, by using strongly bound N-dodecylbenzene sulfonic acid (DBSA). A stable, rigid crystal structure, as well as uniform, orderly-arranged surface of these NPLs is achieved by optimizing intermediate reaction stage, by switching from molecular clusters to mono-octahedra, while interaction with DBSA resulted in formation of a Cs_xO monolayer shell capping the NPL surface. As a result, both structural and optical stability of the $CsPbBr_3$ NPLs is enhanced by strong covalent bonding of DBSA, which inhibits undesired phase transitions and decomposition of the perovskite phase potentially caused by ligand desorption. Moreover, rather small amount of DBSA ligands at the NPL surface results in a short inter-NPL spacing in their closely-packed films, which facilitates efficient charge injection and transport. Blue photoluminescence of the produced $CsPbBr_3$ NPLs is bright (nearly unity emission quantum yield) and peaks at 457 nm with an extremely narrow bandwidth of 3.7 nm at 80 K, while the bandwidth of the electroluminescence (peaked at 460 nm) also reaches a record-narrow value of 15 nm at room temperature. This value corresponds to the CIE coordinates of (0.141, 0.062), which meets Rec. 2020 standards for ultra-high-definition displays.

Introduction

Display and energy-saving lighting applications require blue light-emitting diodes (LEDs) with the Commission Internationale de l'Eclairage (CIE) y-coordinate below 0.15, alongside with the $(x + y)$-value below 0.30[1]. Metal halide perovskites are potential candidates for meeting the requirements of ultra-high definition displays[2] that possess color-saturated blue, green and red emission with CIE coordinates around (0.131, 0.046), (0.170, 0.797), and (0.708, 0.292), respectively, as they exhibit excellent optical properties, such as high photoluminescence quantum yield (PL QY), adjustable bandgap, high color purity, and wide color gamut, and can be produced by low-cost solution processing[3,4]. However, even though significant advances have been made in recent years towards red and green perovskite LEDs which are reaching close to 30% external quantum efficiencies (EQEs)[5–7], it is still difficult to realize spectrally stable, color-saturated blue electroluminescence (EL) for perovskite LEDs[8]. Current efforts at achieving blue emission in perovskite LEDs largely rely on mixed-halide perovskite compositions suffering from ion migration-induced poor color stability[9,10]. Another way to tune the bandgap and

Correspondence: Weijia Zheng (alex610@foxmail.com) or
Xiaoyu Zhang (zhangxiaoyu@jlu.edu.cn) or
Andrey L Rogach (andrey.rogach@cityu.edu.hk)
[1]Key Laboratory of Automobile Materials MOE, School of Materials Science & Engineering, and Jilin Provincial International Cooperation Key Laboratory of High-Efficiency Clean Energy Materials, Jilin University, Changchun, China
[2]State Key Laboratory of Supramolecular Structure and Materials, College of Chemistry, Jilin University, Changchun, China
Full list of author information is available at the end of the article
These authors contributed equally: Qianqian Huang, Wenxu Yin.

the emission color of metal halide perovskites is by taking advantage of the quantum confinement effect while producing respective nanoparticles[11–14], but this approach has its own disadvantages due to the reduced PL QYs caused by increased surface defects upon decreasing size, and poor stability of perovskites due to their low formation energy and ionic nature. Fortunately, surface engineering offers the possibility of passivating defects and obtaining more robust perovskite crystal structures. Surface engineering involves altering the chemical composition of the perovskite surface, which can be realized by introducing organic capping molecules or inorganic ligands[15–23]. On the one hand, this allows for the creation of highly sturdy surface bonding and an orderly arrangement of surface atoms, reducing defects and promoting radiative recombination. On the other hand, this can also enhance the overall structural rigidity of the perovskite crystals, which benefits from the surface strain generated by the ligands for nanostructures with large specific surface areas. There has been evidence that the phase transition point between different crystal phases varies greatly as a function of crystal size in lanthanide elements (e.g., $NaYF_4$), oxides (e.g., TiO_2), metals (e.g., Ag), and ferroelectrics (e.g., $BaTiO_3$)[24–26]. Usually, the smaller the size, the higher the phase transition temperature. Similarly, taking bulk $CsPbI_3$ as an example, the cubic α-phase with a direct bandgap is only stable at high temperatures (>633 K)[27], and transforms into an orthorhombic phase with non-perovskite structure below 593 K[28], whereas $CsPbI_3$ nanoparticles can maintain their cubic phase below 273 K[28]. Thus, utilizing proper surface ligand engineering to optimize the surface structure of quantum-confined $CsPbBr_3$ nanoparticles holds a great potential for achieving efficient and stable blue emitters[29].

Here, we demonstrate how the crystal integrity and structural rigidity of quantum-confined color-saturated blue-emitting $CsPbBr_3$ nanoplatelets (NPLs) can be significantly enhanced via realization of their ordered and stable surface structure using covalently bound molecule N-dodecylbenzene sulfonic acid (DBSA). These $CsPbBr_3$ NPLs show near-unity PL QYs with strong color-saturated blue emission which is peaked at 457 nm PL with an extremely narrow bandwidth of 3.7 nm at 80 K. Blue-emitting LEDs based on these NPLs show stable EL peaking at 460 nm with a record narrow bandwidth of 15 nm at room temperature. This value corresponds to the CIE coordinates of (0.141, 0.062), which meets Rec. 2020 standards for ultra-high-definition displays.

Results

Synthesis of $CsPbBr_3$ NPLs

According to the previous studies[30–32], the surface of $CsPbBr_3$ NPLs is terminated with bromide ions, and each oleylamine (OLA) ligand forms a hydrogen bond with Br^-. We performed density functional theory (DFT) calculations which indicated that the bond energy between Pb^{2+} and Br^- significantly decreases from 2.08 to 1.21 eV after capping OLA-Br, leading to the formation of the vacancy defects and even structural collapse of the perovskite lattice when Br^- ions detach from the surface (Fig. S1). According to the DFT results, the adsorption energy between Pb^{2+} and deprotonated DBSA is 5.16 eV, which falls within the range of binding energies ranging from 3.1 to 8.2 eV for covalent bonds (Fig. S1), indicating that DBSA ligands are covalently bound due to the benzenesulfonic group's high acidity and electron-withdrawing ability. Therefore, DBSA ligands can be used to achieve stable surface structures on $CsPbBr_3$ NPLs, eventually able to prevent ligand desorption, inhibit ionic migration, and improve the crystal stability.

Perovskite nanocrystals can be synthesized using a variety of techniques, including ligand-assisted reprecipitation (LARP), hot injection, ultrasonication, microwaves, solvothermal, and saponification[33–35]. Among them, the LARP approach relies on changes in solubility of perovskite precursors[36,37], while others require energy supplies, such as thermal or ultrasonic energy, to trigger the chemical reaction between the precursors. In this study, a modified LARP synthesis at room temperature has been employed to obtain $CsPbBr_3$ NPLs capped with DBSA ligands (see Materials and methods for details). As a first step, $PbBr_2$ dissolved in dimethyl sulfoxide (DMSO) is injected into a mixture solution containing oleic acid (OA), OLA, and toluene, with or without DBSA. When DBSA is absent in this mixture, $PbBr_2$-OLA molecular clusters and $[Pb_nBr_{3n}]^{n-}$ chains ($n > 1$) are formed, as illustrated in Fig. 1, upper part. This assumption follows from the pronounced absorption at 396 nm which belongs to molecular clusters[38], while absorption ranging from 350 to 380 nm indicates the formation of $[Pb_nBr_{3n}]^{n-}$ chains (Fig. S2), which is consistent with previous studies[39]. In contrast, when DBSA is present, there is no absorption peak at 396 nm (Fig. S2), suggesting that the formation of molecular clusters is inhibited due to the strong interaction between DBSA and Pb^{2+} (Fig. S1), resulting in the conversion of molecular clusters into smaller intermediate state structures, namely the mono-octahedra of $PbBr_aDBSA_b^{4-}$ ($a + b = 6$), whose absorption extends into the ultraviolet region. At the same time, the absorption at 350–380 nm (Fig. S2) still indicates the presence of $[Pb_nBr_{3n}]^{n-}$ chains, as illustrated in Fig. 1, bottom part. Also, the presence of DBSA does not cause any additional absorption peaks to appear (Fig. S2), suggesting that no new intermediates are generated in the reaction.

In the second step, the CsBr precursor is injected, which results in a Br-rich environment. In the more tightly arranged face-sharing octahedrons, Br^- ions have higher

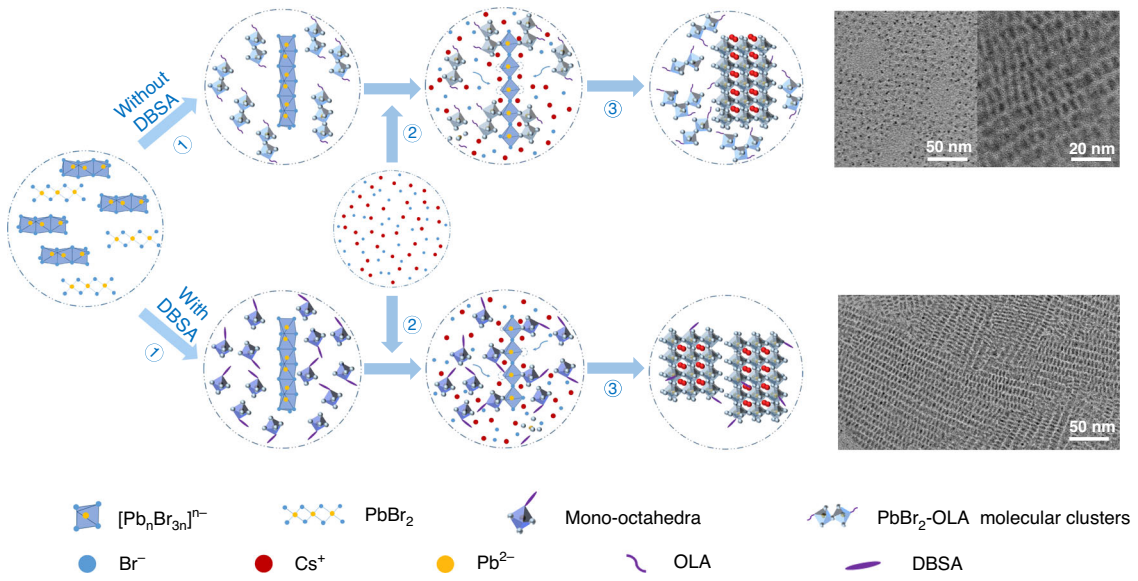

Fig. 1 Growth mechanism analysis. Schematic illustration of the growth mechanism for $CsPbBr_3$ NPLs synthesized without (upper part) and with the use of DBSA (bottom part), and their corresponding TEM images provided on the right

energies than in the corner-sharing octahedrons due to an enhanced repulsive force between the adjacent Pb^{2+}. Pauling's third rule states that octahedrons accommodating cations tend to share corners rather than faces to increase distances and reduce repulsive forces. Thus, this transforms the face-sharing $[Pb_nBr_{3n}]^{n-}$ chains into corner-sharing $[Pb_nBr_{5n}]^{3n-}$ octahedron chains[40]. In the presence of Cs^+, these corner-sharing chains are able to adsorb surrounding molecular clusters or mono-octahedra on their sides, inducing continuous crystal growth to generate $CsPbBr_3$ NPLs. Those mono-octahedra can serve as intermediate states more conveniently than molecular clusters, and they can be arranged more orderly on the NPL surface structure. In the absence of DBSA, as a result of the fast crystallization process, synthesized $CsPbBr_3$ NPLs have rather poor crystallinity and low uniformity of size and shape, as shown by the transmission electron microscopy (TEM) images in Fig. 1 at the top right. In the presence of highly viscous DBSA, the diffusion of mono-octahedra is slow, causing slow crystallization which results in an improved crystallinity of the $CsPbBr_3$ NPLs; they are now characterized by high uniformity of shape and thickness (bottom right of Fig. 1).

For the eventual large-scale synthesis of perovskites, a primary prerequisite is the preservation of emission efficiency, color purity, and crystal quality of the final materials. A demonstration of the scaled-up synthesis has been conducted in our laboratory using 10 times larger volume (50 mL) than in the standard lab-scale synthesis (5 mL). It is apparent from Fig. S3a and S3b that the emission efficiency of $CsPbBr_3$ NPLs remains unchanged even when the reaction volume has been increased by 10 times. When compared to the lab-level synthesis, the almost identical absorption, PL spectra and crystal structure of the $CsPbBr_3$ NPLs suggest that high color purity and crystallinity can indeed be maintained (Figs. S3c and 3d).

In addition, thermal stability and the detrimental influence of polar solvents are considered to be significant factors affecting the properties of perovskite nanocrystals[41]. To check on those factors, according to the previous research[42,43], temperatures ranging from 288 to 328 K and 10 μL of water additives have been chosen, which can easily convert blue emission of perovskite nanocrystals into green emission. The PL spectra and XRD patterns of DBSA-$CsPbBr_3$ NPLs synthesized under the mentioned conditions are not affected at all (Fig. S4), demonstrating the robustness of the DBSA engineering approach against the conditions tested. Besides of the robustness, large-scale synthesis of perovskites also requires consideration of the cost-effectiveness. The price of DBSA is ~29 \$ kg^{-1}, less than that of OA (87 \$ kg^{-1}) and OLA (50 \$ kg^{-1}). Therefore, replacing those two conventional ligands with DBSA to optimize the perovskite quality is in line with potential commercialization objectives. As a room-temperature synthesis method, another advantage of the DBSA engineering approach is that it does not require vacuum equipment, precise temperature control, or expensive inert gases to protect the reaction environment, making it suitable for producing high-quality perovskite nanocrystals on a large scale.

Simple and flexible operation methods can significantly reduce instrument costs and production times, and thus this synthetic approach has significant commercialization potential.

Surface chemical composition

To investigate their surface chemical composition, Fourier transform infrared spectroscopy (FTIR), 1H nuclear magnetic resonance (1H NMR), and X-ray photoelectron spectroscopy (XPS) measurements were conducted on purified $CsPbBr_3$ NPLs synthesized with and without DBSA ($CsPbBr_3$ NPLs produced with DBSA will be denoted as DBSA-$CsPbBr_3$ NPLs in the forthcoming discussion, in order to distinguish them from the notation $CsPbBr_3$ NPLs which will be used for the reference samples made without DBSA), which were obtained by centrifugation after adding methyl acetate. In the FTIR spectra provided in Fig. 2a, peaks of DBSA-$CsPbBr_3$ NPLs at 1602, 1576, and 1495 cm^{-1} are associated with benzene stretching vibrations[44]; those peaks are absent in FTIR spectra of $CsPbBr_3$ NPLs. Peaks at 1038, 1007, and 680 cm^{-1} seen in DBSA-$CsPbBr_3$ NPLs belong to the S=O and S–O stretching vibrations of the sulfonate group ($-SO_3^-$)[45], respectively, and the peak at 582 cm^{-1} is the tensile vibration of S–C[46]. The presence of all those characteristic vibration peaks indicates that the deprotonated DBSA is bound to the $CsPbBr_3$ NPL surface. In the 1H NMR spectra shown in Fig. 2b, DBSA-$CsPbBr_3$ NPLs possess five resonance peaks associated with DBSA containing six characteristic hydrogens, while the absence of resonance peak around 11 ppm indicates that the deprotonated sulfonic acid groups bind to Pb^{2+} at the DBSA-$CsPbBr_3$ NPL surface. Furthermore, the prominent chemical shift towards the low-field, and a significant hydrogen peak broadening suggest a strong interaction between DBSA and $CsPbBr_3$ NPLs[47], which is also supported by the FTIR data (Fig. 2a). As judged from the FTIR and NMR spectra, the deprotonated sulfonic acid groups of DBSA are bound to the NPL surface, because DBSA has a greater bonding energy than OLA-Br. This is because DBSA is a soft X-type ligand, which has a strong affinity for binding to undercoordinated Pb^{2+} than hard X-type ligands such as OLA-Br, donating one electron to a halide anion.

XPS spectra further confirm the strong ligand-surface interaction in DBSA-$CsPbBr_3$ NPLs, as opposed to the $CsPbBr_3$ NPLs. Figure S5a shows the fitting for XPS peaks of S *2p* at 163.9 eV, 162.6 eV, and 161.3 eV, which correspond to S-C_6H_4-, S=O and S–O bonds, respectively. Figure S5b shows the fitting for XPS peaks of O *1s* at 531.7 eV and 529.4 eV corresponding to O–S and Pb–O, respectively; they match those in OA passivated perovskite nanocrystals[48]. Through the S–O–Pb bonds, DBSA ligands are tightly bound to the NPL surface. As compared to $CsPbBr_3$ NPLs, the two distinctive peaks of Pb *4f* and Br *3d* are shifted to higher binding energy in DBSA-$CsPbBr_3$ NPLs: from 143.1 and 138.2 eV to 143.4 and 138.6 eV for Pb *4f*, and from 68.9 and 67.9 eV to 69.3 eV and 68.3 eV for Br *3d*, respectively (Figs. 2c and 2d)[49]. This can be attributed to electron transfer from Pb^{2+} ions to ligands in DBSA-$CsPbBr_3$ NPLs, due to the high adsorption energy between Pb^{2+} and deprotonated DBSA. As deducted from Fig. 2e, the atomic ratios of Pb-to-Br determined from XPS data is 1/2.7 in $CsPbBr_3$ NPLs which is larger than the atomic ratio of Pb/(Br+S) equal to 1/3.3 in DBSA-$CsPbBr_3$ NPLs (here, the S-content serves as an indicator of the amount of DBSA), suggesting that the uncoordinated Pb^{2+} have been fully passivated at the surface of the latter. All these data point out towards the formation of a stable and ordered surface structure in the case of in DBSA-$CsPbBr_3$ NPLs, which enhances their structural rigidity.

A shift to higher binding energy in the XPS spectra of Cs *3d* in DBSA-$CsPbBr_3$ NPLs is also detected (Fig. S5c), whereas conventional surface engineering for passivating surface Br-vacancy is not able to alter the bonding energy of Cs^+ since these cations are located at the center of four $[PbBr_6]^{4-}$ octahedral, and thus do not participate in the orbital hybridization[50]. We employ DFT calculations (Fig. 2f, g) to identify the possible reason for the observed shift of the Cs *3d* XPS peaks. Unlike OLA ligands that only interact with one Pb^{2+} cation, DBSA can also form chemical bonds with three surrounding Cs^+, with bond lengths of 2.91, 3.11, and 3.25 Å (Fig. S6), respectively, which is almost equivalent to the bonds formed in Cs_xO, where the bond length is 2.86 Å[51]. Gain and lose of the electrons, and the electron density transfer between Cs and O atoms can be obtained from the Bader charge calculation (Table S1) and be seen from the charge density difference shown in Fig. 2h for DBSA-$CsPbBr_3$ surface, which corresponds to the formation of chemical bonds. Thus, the surface of the DBSA-$CsPbBr_3$ NPLs can be thought to be coated with a monolayer of Cs_xO shell, which increases the overall Cs^+ binding energy, stabilizes the surface and improves the structural rigidity of these NPLs.

Due to the multiple coordination between the DBSA ligands and the NPL surface (one Pb^{2+} and three Cs^+) and the branched chains oriented parallel to the NPL surface, which is caused by ortho-substituted benzene of DBSA (Fig. 2g and Fig. S6b), DBSA-$CsPbBr_3$ NPLs experience a lower ligand surface coverage as compared to $CsPbBr_3$ NPLs, and thus show a shorter spacing distance than the latter in their close-packed films, as has been confirmed by the following TEM data. As opposed to the $CsPbBr_3$ NPLs with uneven size and shape distribution (Fig. S7a and Fig. 1), DBSA-$CsPbBr_3$ NPLs show much more uniform size and shapes (Fig. S7b and Fig. 1),

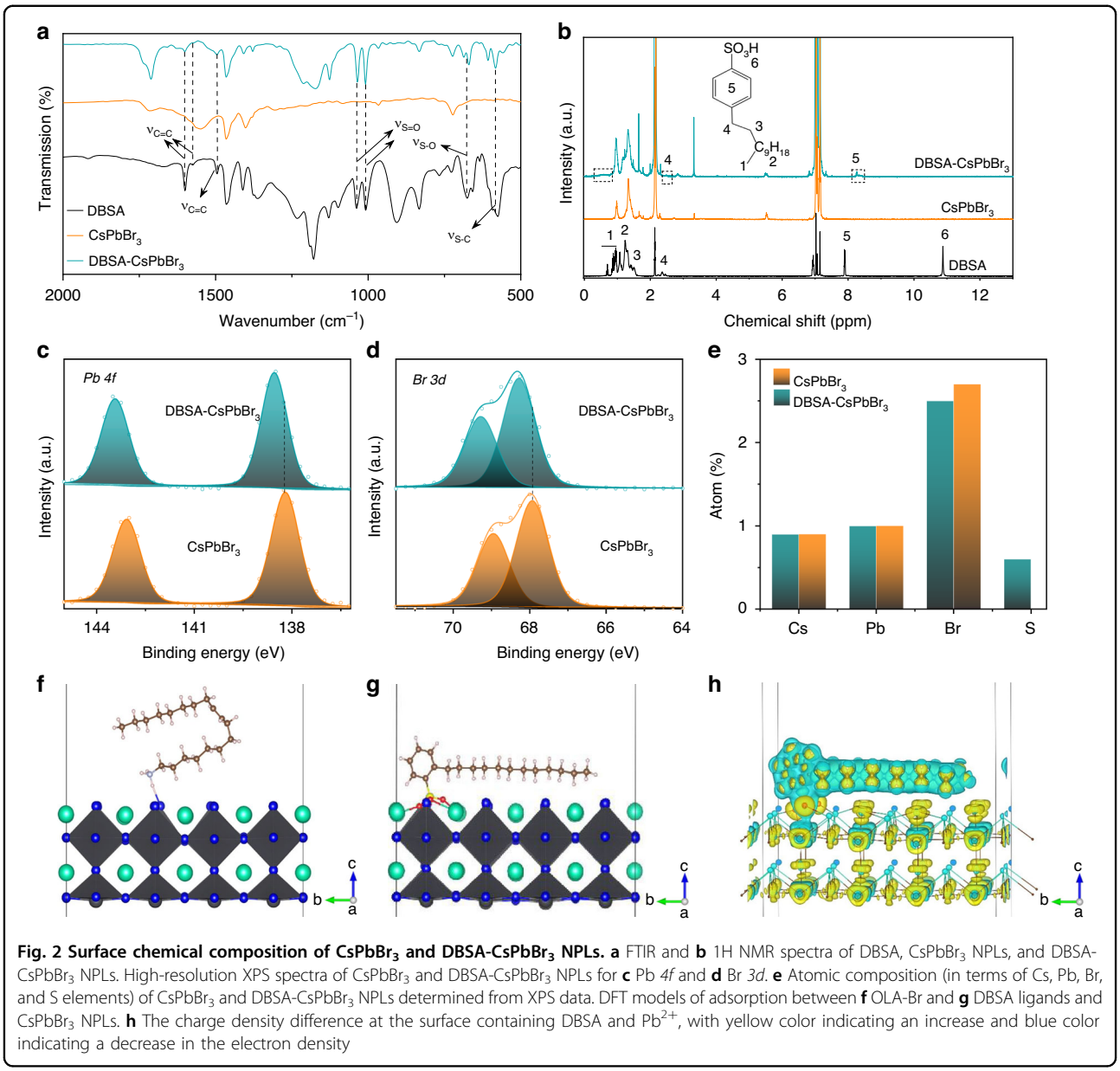

Fig. 2 Surface chemical composition of $CsPbBr_3$ and DBSA-$CsPbBr_3$ NPLs. a FTIR and **b** 1H NMR spectra of DBSA, $CsPbBr_3$ NPLs, and DBSA-$CsPbBr_3$ NPLs. High-resolution XPS spectra of $CsPbBr_3$ and DBSA-$CsPbBr_3$ NPLs for **c** Pb *4f* and **d** Br *3d*. **e** Atomic composition (in terms of Cs, Pb, Br, and S elements) of $CsPbBr_3$ and DBSA-$CsPbBr_3$ NPLs determined from XPS data. DFT models of adsorption between **f** OLA-Br and **g** DBSA ligands and $CsPbBr_3$ NPLs. **h** The charge density difference at the surface containing DBSA and Pb^{2+}, with yellow color indicating an increase and blue color indicating a decrease in the electron density

with two kinds of close-packing observed on the TEM images: NPLs either lying side-by-side or stacking face-to-face. In Fig. S7c, high-resolution TEM (HRTEM) image reveals cubic structure for DBSA-$CsPbBr_3$ NPLs with 0.59 nm lattice spacing corresponding to the (100) plane[52]. From the statistical analysis of 100 particles, DBSA-$CsPbBr_3$ NPLs have a thickness of ~1.9 nm, an edge length of ~6.2 nm, and an interparticle distance of ~2.3 nm between closely-packed NPLs (Fig. S7d–f). Considering the height of a $[PbBr_6]^{4-}$ octahedra in the perovskite structure being equal to 0.59 nm, the number of unit-cells in the DBSA-$CsPbBr_3$ NPLs should be equal to 3.

Crystallinity and structural stability

X-ray diffraction (XRD) measurements are conducted on drop-cast $CsPbBr_3$ and DBSA-$CsPbBr_3$ NPL films. Both kinds of NPLs exhibit strong diffraction peaks in small-angle XRD patterns (Fig. S8), which reflect the interplanar diffraction peaks of (002), (004), and (006) from the face-to-face stacking of the NPLs[53]. XRD patterns also confirm that the DBSA-$CsPbBr_3$ NPL films are more orderly assembled as compared to $CsPbBr_3$ NPL films, which results in a higher periodicity of the peaks at small angles. The diffraction peaks from $CsPbBr_3$ and DBSA-$CsPbBr_3$ NPL stacking appear at regular intervals of $\Delta 2\theta = 2.1°$ and 2.2°, respectively, corresponding to the

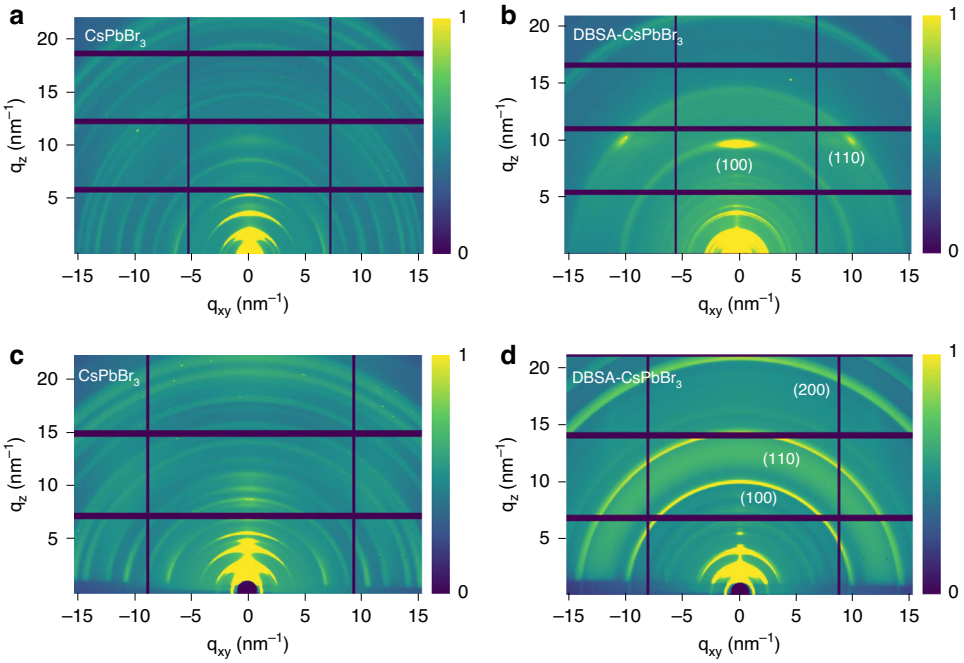

Fig. 3 Structural characterization of $CsPbBr_3$ and DBSA-$CsPbBr_3$ NPLs. 2D GIWAXS patterns of **a** $CsPbBr_3$ and **b** DBSA-$CsPbBr_3$ NPLs, and 2D GIXRD patterns of **c** $CsPbBr_3$ and **d** DBSA-$CsPbBr_3$ NPLs

spacing between face-to-face NPLs equal to 4.2 and 4.1 nm, respectively.

Combining grazing incidence wide-angle X-ray scattering (GIWAXS) and grazing incidence X-ray diffraction (GIXRD) measurements, we have further analyzed the structural details of $CsPbBr_3$ and DBSA-$CsPbBr_3$ NPL films. Spacings associated with the low-q peaks (namely diffraction peaks less than 10 nm^{-1}) identify the periodic structure reflecting NPL placement[54], while the high-q peaks reveal the crystal structure of $CsPbBr_3$ perovskites. From GIWAXS patterns (Fig. 3a, b), equally spaced scattering rings of low-q values are recognized for both kinds of NPLs, indicating that they all possess periodic structures. As compared to the $CsPbBr_3$ NPL films, DBSA-$CsPbBr_3$ NPL films exhibit a preferential orientation with the appearance of strong, sharp, and discrete Bragg spots in the (110) and (100) planes. Such preferential orientation of DBSA-$CsPbBr_3$ NPLs can be ascribed to their uniform morphology (Fig. 1), better monodispersity and reduced spatial hindrance when compared with the $CsPbBr_3$ NPLs with various morphologies and various folding/bending forms of OLA-Br (DFT results shown in Figs. 2f and 2g), allowing for an orderly arrangement in films. In addition, the scattering intensity of the out-of-plane direction (q_z) in DBSA-$CsPbBr_3$ NPL films is much higher than that of the in-plane direction (q_{xy}), suggesting that DBSA-$CsPbBr_3$ NPLs are preferentially oriented parallel to the substrate (Fig. 3b). Data from the GIXRD measurements performed on the $CsPbBr_3$ and DBSA-$CsPbBr_3$ NPL films are presented in Figs. 3c and 3d, respectively. Similar to GIWAXS data, both films exhibit diffraction rings of relatively greater intensity along the q_z than the q_{xy} axis, indicating their preference for parallel orientation. The diffraction ring intensity for $CsPbBr_3$ NPLs is strong only for the low-q peaks, while for DBSA-$CsPbBr_3$ NPLs, it is also strong for the (100), (110), and (200) planes, suggesting much-improved crystallinity.

As enhanced crystal quality increases NPL resistance to external stimuli, we expect DBSA-$CsPbBr_3$ NPLs to have higher stability. XRD patterns of the two samples are thus compared after storing them at ambient conditions for different period of time. Unlike films made of $CsPbBr_3$ NPLs which decomposed completely within 10 days as judged from the XRD data (Fig. S9a), DBSA-$CsPbBr_3$ NPL films maintain their original XRD patterns after 40 days of storage (Fig. S9b), indicating their enhanced stability. We also evaluate the PL stability of $CsPbBr_3$ and DBSA-$CsPbBr_3$ NPLs in films, freshly prepared and stored for different time periods under 40% relative humidity, as summarized in Fig. S9c. While both the PL peak position and PL bandwidth of the DBSA-$CsPbBr_3$ NPL films remain almost unchanged after 15 days, the PL peak of $CsPbBr_3$ NPL films red-shift by 13 nm to 472 nm, and a shoulder peak appears at 497 nm after 5 days of storage. As can be seen from the

photographs of those films shown in Fig. S10, the $CsPbBr_3$ NPL films lose their blue PL emission much faster than DBSA-$CsPbBr_3$ NPL films.

Figure S11 provides the data related to evaluation of UV irradiation and thermal stability of $CsPbBr_3$ and DBSA-$CsPbBr_3$ NPLs. The PL intensities of $CsPbBr_3$ and DBSA-$CsPbBr_3$ NPL films decline to ~50% after continuous UV illumination for 4 min and 28 min (Fig. S11a), respectively, indicating a seven-fold increase of the half-life under UV illumination for the DBSA-$CsPbBr_3$ NPLs. Figure S11b shows the thermal stability of the two kinds of NPL films, measured from 293 to 353 K. Upon reaching 353 K, $CsPbBr_3$ and DBSA-$CsPbBr_3$ NPL films lose 93% and 68% of their peak PL intensity, respectively. During the heating process, the PL spectra from DBSA-$CsPbBr_3$ NPL film remain almost unchanged, while the PL spectra of $CsPbBr_3$ NPL film shift from 463 to 490 nm as a result of the NPL aggregation. Consequently, the DBSA-$CsPbBr_3$ NPL films show improved stability both towards UV irradiation and heat.

Optical properties

Steady-state absorption and PL spectra of the two kinds of NPLs are shown in Fig. 4a. Because of the highly dynamic OLA-Br binding of $CsPbBr_3$ NPLs, OLA and $PbBr_2$ are generated upon decomposition of the NPL surface. Over time, OLA and $PbBr_2$ concentration in solution would increase, causing molecular clusters to form again. Therefore, some molecular cluster absorption at 396 nm can still be detected in $CsPbBr_3$ NPLs. Compared with $CsPbBr_3$ NPLs, the absence of strong absorption at 396 nm in DBSA-$CsPbBr_3$ NPLs indicates that the molecular clusters as impurities have been inhibited completely. Also in absorption, DBSA-$CsPbBr_3$ NPLs exhibit a slight red shift of 4 nm of their first excitonic peak, as compared to $CsPbBr_3$ NPLs, and an additional peak at 403 nm appears originating from higher-energy transition, which could only be observed in highly quantum-confined perovskite NPLs with a small Stokes shift and uniform morphology[55–57]. The PL maxima of $CsPbBr_3$ and DBSA-$CsPbBr_3$ NPLs are located around 460 nm, which corresponds to three vertically stacked unit-cells in NPLs. The Urbach tail is an indication of structural and electronic disorder in luminescent materials, and the Urbach energy (E_U) is calculated to quantify the band edge broadening, according to the formulae $\alpha = \alpha_0 \exp[(h\nu - E_g)/E_U]$, where α is the absorption coefficient as a function of photon energy, $h\nu$ is the photon energy, E_g—the optical bandgap, and α_0 is a constant. From Fig. S12, the E_U for $CsPbBr_3$ NPLs is 27 meV, while for DBSA-$CsPbBr_3$ NPLs it is much lower, namely 19 meV. This shows that DBSA-$CsPbBr_3$ NPLs are less electronically disordered and have a lower trap density than $CsPbBr_3$ NPLs[58].

Figures 4b and c show pseudocolor maps of the temperature-dependent PL for $CsPbBr_3$ and DBSA-$CsPbBr_3$ NPLs, respectively, collected for the temperature range of 80–220 K. There is almost no shift in the PL peak for the both kinds of NPLs as the temperature increases. The DBSA-$CsPbBr_3$ NPLs at 80 K have a bandwidth of 3.7 nm, which is much narrower than 8 nm of $CsPbBr_3$ NPLs, again suggesting fewer electronic/structural disorder and scattering on defects (Fig. S13)[59–62]. When the temperature increases to 220 K, the PL bandwidth increases to 8 nm for DBSA-$CsPbBr_3$ NPLs as compared to 11 nm for $CsPbBr_3$ NPLs. Stronger change of the temperature-dependent PL bandwidth observed for the DBSA-$CsPbBr_3$ NPLs indicates that excitonic recombination dominates at lower temperatures, demonstrating superior crystal quality of this sample[63].

$CsPbBr_3$ and DBSA-$CsPbBr_3$ NPLs are further characterized using time-resolved PL (TRPL) spectroscopy, and their PL QYs are determined. Bi-exponential and the mono-exponential decays are used to fit the TRPL decay curves of $CsPbBr_3$ NPLs and DBSA-$CsPbBr_3$ NPLs, respectively (Fig. 4d). According to Table S2, the average PL lifetime (τ_{ave}) increases from 1.8 ns in $CsPbBr_3$ NPLs to 4.0 ns in DBSA-$CsPbBr_3$ NPLs. Under 365 nm excitation, the PL QY of DBSA-$CsPbBr_3$ NPLs reaches impressive 97% at room temperature in toluene solution, which is much higher than 10% in $CsPbBr_3$ NPLs. Recombination rates for radiative (K_r) and nonradiative (K_{nr}) are calculated by using equations $K_r = PLQY/\tau_{ave}$ and $K_{nr} = 1/\tau_{ave} - K_r$, and the obtained values are summarized in Table 1. K_r of DBSA-$CsPbBr_3$ NPLs increases 4-fold as compared to $CsPbBr_3$ NPLs, while K_{nr} decreases 72-fold, which is due to the crystallinity and structural rigidity improvements brought out by using DBSA, which prevent the defect formation and thus eliminates nonradiative recombination.

Femtosecond transient absorption (TA) spectra are used to examine the carrier dynamics of $CsPbBr_3$ and DBSA-$CsPbBr_3$ NPLs. Both kinds of NPLs exhibit photobleaching at 455 nm (Fig. 4e, f), which corresponds to the ground-state bleaching of the first excitonic transition. The photobleaching peak caused by molecular clusters is observed at 393 nm for $CsPbBr_3$ NPLs, but not for DBSA-$CsPbBr_3$ NPLs, in accordance with their absorption spectra (Fig. 4a). As shown in Fig. 4g, DBSA-$CsPbBr_3$ NPLs have slower decay dynamics than $CsPbBr_3$ NPLs, which is consistent with TRPL data discussed above. A more detailed picture of the carrier dynamic processes is revealed by decay-associated TA spectra, which are shown in Fig. 4h, i. The related time constants are extracted as follows: $\tau_1 = 1.7$ ps, $\tau_2 = 13.1$ ps, $\tau_3 > 1$ ns for DBSA-$CsPbBr_3$ NPLs, and $\tau_1 = 1.8$ ps, $\tau_2 = 125.2$ ps, $\tau_3 > 1$ ns, $\tau_4 = 5.3$ ps for $CsPbBr_3$ NPLs. Here, τ_1, τ_2, and τ_3 account for intraband hot-exciton relaxation, exciton trapping in

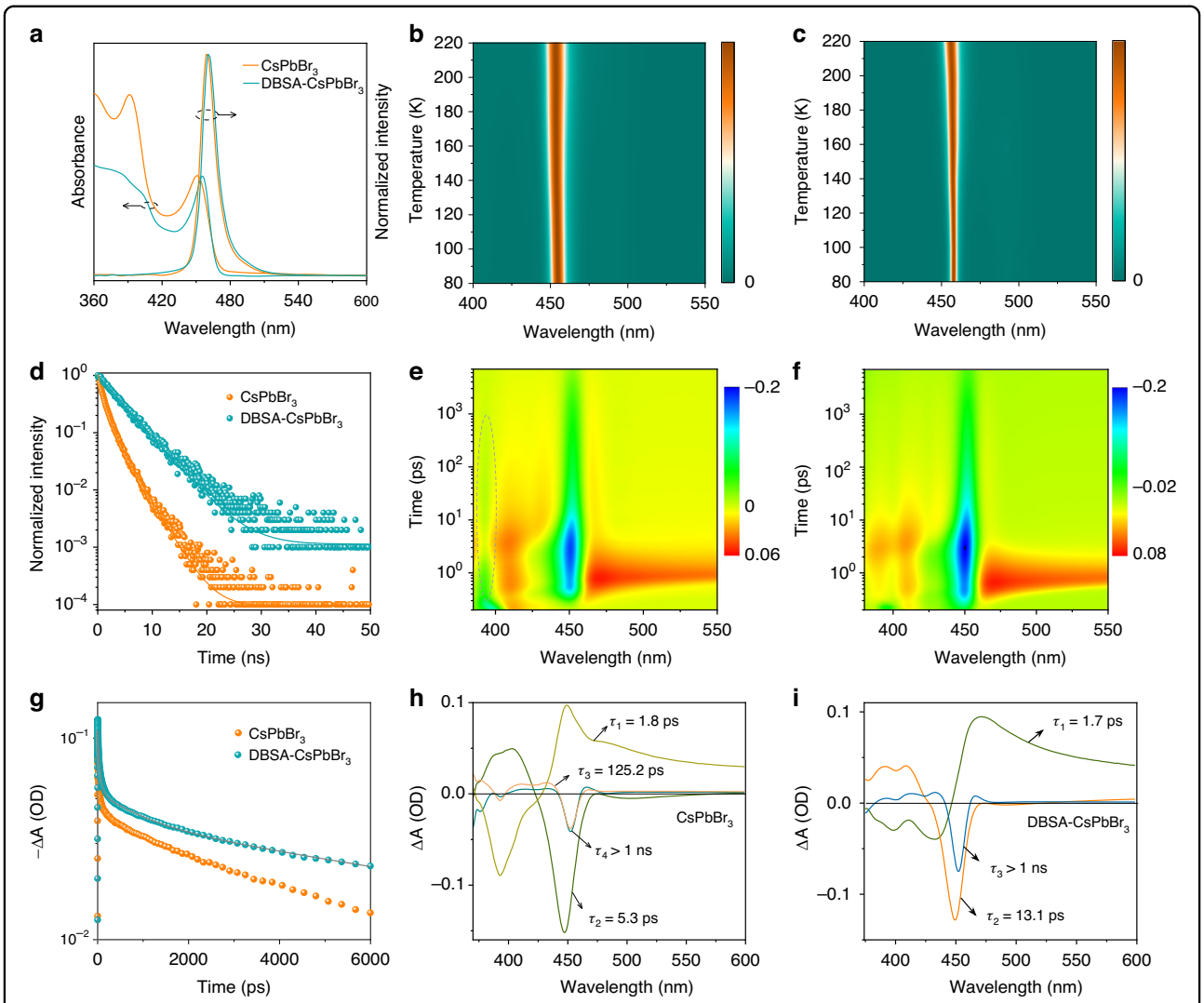

Fig. 4 Optical properties of $CsPbBr_3$ and DBSA-$CsPbBr_3$ NPLs. a Steady-state absorption and PL spectra (365 nm excitation) of $CsPbBr_3$ and DBSA-$CsPbBr_3$ NPLs dissolved in toluene. Pseudocolor spectral map of temperature-dependent PL measured from 80 K to 220 K of **b** $CsPbBr_3$ and **c** DBSA-$CsPbBr_3$ NPLs. **d** Time-resolved PL decay curves of $CsPbBr_3$ and DBSA-$CsPbBr_3$ NPLs. TA plots of **e** $CsPbBr_3$ and **f** DBSA-$CsPbBr_3$ NPLs. **g** Comparison of the bleach recovery kinetics of $CsPbBr_3$ and DBSA-$CsPbBr_3$ NPLs measured at 455 nm. Characteristic decay-associated TA spectra for **h** $CsPbBr_3$ and **i** DBSA-$CsPbBr_3$ NPLs

Table 1 PL QYs, radiative recombination rates (K_r), and nonradiative recombination rates (K_{nr}) of $CsPbBr_3$ and DBSA-$CsPbBr_3$ NPLs

Sample	PL QY (%)	K_r ($\times 10^7$ s^{-1})	K_{nr} ($\times 10^7$ s^{-1})
$CsPbBr_3$	10	5.6	50.0
DBSA-$CsPbBr_3$	97	24.3	0.7

the bandgap trap states, and exciton recombination, respectively[7,64]. The former two processes are faster in DBSA-$CsPbBr_3$ NPLs than in $CsPbBr_3$ NPLs, suggesting that their enhanced crystal rigidity indeed lowers the defect density and suppresses electron-phonon coupling[65,66]. Besides, the τ_4 component which is only present in $CsPbBr_3$ NPLs represents the energy transfer from molecular clusters to $CsPbBr_3$ NPLs; this component is absent in DBSA-$CsPbBr_3$ NPLs.

$CsPbBr_3$ NPL-based LEDs

For the demonstration of the benefits of enhanced structural rigidity, both kinds of perovskite NPLs have been used as emitter layers in LEDs, in order to compare their EL performance. Figure 5a illustrates the LED architecture, which includes indium tin oxide (ITO)/poly-(ethylene dioxythiophene):polystyrene sulfonate (PEDOT:PSS)/poly (N,N9-bis(4-butylphenyl)-N,N9-bis(phenyl)-

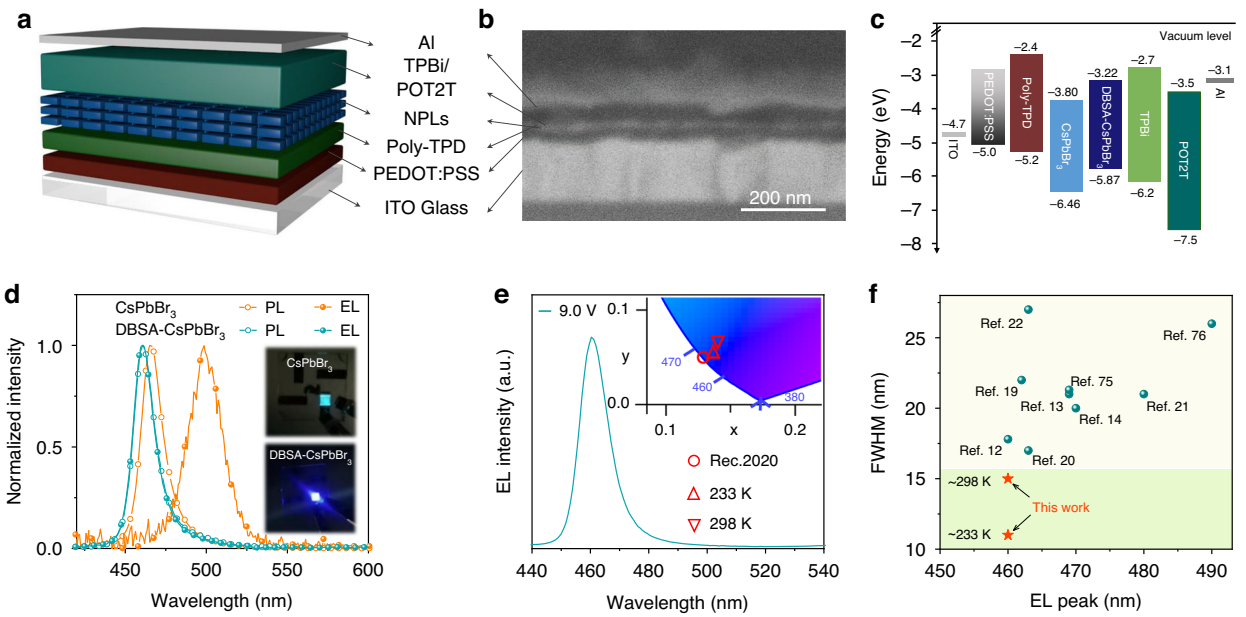

Fig. 5 NPL-based LEDs. a Schematic illustration of the NPL-based LED structure, **b** its corresponding cross-sectional SEM image, and **c** its energy band diagram. **d** EL spectra of the LEDs based on $CsPbBr_3$ and DBSA-$CsPbBr_3$ NPLs (curves labeled with filled circles) and PL spectra of the respective NPL films (curves labeled with open circles). The insets show photographs of the LEDs based on $CsPbBr_3$ and DBSA-$CsPbBr_3$ NPLs operated under a 7 V bias. **e** EL spectrum of the DBSA-$CsPbBr_3$ NPL-based LED operated at 233 K. The inset shows the CIE coordinates of the devices operated at 233 and 298 K, which are compared with the Rec. 2020 CIE coordinates for blue light applied for ultra-high-definition displays. **f** Comparison of the EL bandwidth of the reported blue LEDs based on $CsPbBr_3$ and $(CsPbCl_xBr_{1-x})_3$ NPLs and nanocrystals, and the values obtained for our DBSA-$CsPbBr_3$ NPL-based LED at 233 and 298 K[12–14,19–22,75,76]

benzidine) (Poly-TPD)/polyethyleneimine (PEI)/NPLs/1,3,5-Tris(1-phenyl-1H-benzimidazol-2-yl)benzene (TPBi)/2,4,6-Tris[3-(diphenylphosphinyl)phenyl]-1,3,5-triazine (POT2T)/Al. Here, the ITO substrate serves as the anode, a bilayer of PEDOT: PSS/Poly-TPD with a thickness of ~30 nm—as the hole transport layer (HTL), the layer of $CsPbBr_3$ NPLs (~12 nm)—as the emitting layer, a bilayer of TPBi/POT2T (~40 nm)—as the electron transport layer (ETL), and Al layer (~100 nm)—as the cathode. A scanning electron microscope (SEM) in Fig. 5b visualizes the device structure and the thicknesses of each functional layer.

Ultraviolet photoelectron spectroscopy (UPS) is used to determine the valence band maximum (VBM) and the Fermi energy level (E_F) for both kinds of perovskite NPLs. For the DBSA-$CsPbBr_3$ NPLs, the VBM upshifts from −6.46 to −5.87 eV as compared to the reference $CsPbBr_3$ NPLs, while the E_F downshifts from −3.90 to −3.47 eV (Fig. S14a). Consequently, emitting layers of DBSA-$CsPbBr_3$ NPLs have higher hole concertation than of the $CsPbBr_3$ NPLs resulting in a faster hole transport recorded from the "hole-only" devices of Fig. S15. Moreover, for the films made of DBSA-$CsPbBr_3$ NPLs, the hole injection barrier decreases from 1.26 to 0.67 eV as compared to the films of $CsPbBr_3$ NPLs (Fig. 5c). From the Tauc plots of the perovskite films on quartz substrates provided in Fig. S14b, the bandgap values of $CsPbBr_3$ and DBSA-$CsPbBr_3$ NPLs are determined as 2.68 eV and 2.67 eV, respectively. The upward moving conduction band minimum (CBM) reduces the energy level difference between the ETL and the emitting layer by 0.58 eV in the LED based on DBSA-$CsPbBr_3$ NPLs (Fig. 5c), which should result in a more reliable and stable LEDs. Space-charge limited-current measurements are performed on the hole-only and electron-only devices (with the device structure provided in Fig. S14 caption) to further demonstrate the advantages of the surface engineering using DBSA. When operated at low voltages, the current density in the hole-only devices based on DBSA-$CsPbBr_3$ NPLs is higher, while in their electron-only devices it is lower, which suggests an improved charge balance in LEDs as compared to respective devices based on $CsPbBr_3$ NPLs. Meanwhile, the current density-voltage curve for the $CsPbBr_3$ NPL hole-only device increases sharply under high voltage, which is a signature of the material degradation. Hole and electron trap-filled limit voltages (V_{TFL}) of the devices based on DBSA-$CsPbBr_3$ NPLs (0.91 and 2.02 V) are both lower than those based on $CsPbBr_3$ NPLs (1.15 and 2.40 V). Moreover, DBSA-$CsPbBr_3$ NPLs show lower trap density than $CsPbBr_3$ NPLs (Table S3), which is in a good agreement with removal of the surface defects by the treatment with DBSA.

From the current density-voltage-luminance (*J-V-L*) curves shown in Fig. S16a, DBSA-$CsPbBr_3$ NPL-based LEDs exhibit a lower turn-on voltage (3.0 V), as well as higher current densities and brightness than the LED based on $CsPbBr_3$ NPLs. While the $CsPbBr_3$ NPL-based LEDs show external quantum efficiency (EQE) of only 0.08% and the brightness of 55 cd m^{-2}, the DBSA-$CsPbBr_3$ NPL-based LEDs with the respective values of 1.60% and 591 cd m^{-2} are 20 times more efficient and more than 10 times brighter (Fig. S16b). Importantly, the averaged EQE value recorded for 30 DBSA-$CsPbBr_3$ NPL-based LEDs is 1.22% (Fig. S17), demonstrating high reproducibility. In terms of the device stability, the EL spectrum red-shifts from 465 nm (PL of the film) to 500 nm and the bandwidth broadens to 24 nm from 16 nm in LEDs using $CsPbBr_3$ NPLs (Fig. 5d), so that the emission color of the operating device changes from blue to green (inset in Fig. 5d), which is due to the poor thermal stability (Fig. S11b, c). Because the electron transport layer TPBi is directly deposited on top of the NPL film via thermal evaporation, high temperature vapor facilities the detachment of ligands, leading to the $CsPbBr_3$ NPL aggregation. In contrast, the DBSA-$CsPbBr_3$ NPL-based LEDs show spectrally symmetrical, homogeneous, and bright color-saturated blue emission peaked at 460 nm, with an excellent color stability as demonstrated in Fig. 5d, which is due to the stable NPL surface resulting from strongly bound DBSA. Furthermore, benefitting from the superior structural stability of the DBSA-$CsPbBr_3$ NPLs, when the voltage increases from 4.5 to 6.5 V, the EL peak and bandwidth of the color-saturated blue LEDs remain almost unchanged (Fig. S18), indicating that the color purity and CIE coordinates are not affected. Thus, the device's EL meets the standard for high-definition displays throughout their operation. By comparison with the reported blue LEDs based on $CsPbBr_3$ and $CsPb(Cl_xBr_{1-x})_3$ NPLs and nanocrystals provided in Fig. 5f, DBSA-$CsPbBr_3$ NPL LEDs have the narrowest EL bandwidth of 15 nm at 298 K and 11 nm at 233 K. Since DBSA-$CsPbBr_3$ NPLs with superior crystal quality possess fewer electronic defects or structural disorders, phonon scattering is suppressed at low temperatures, so that the excitonic recombination characterized by a narrow emission bandwidth dominates. The EL spectra at 298 K and 233 K corresponds to CIE coordinates of (0.141, 0.062) and (0.138, 0.050), resulting in CIE *y*-coordinate values of 0.062 and 0.050 below 0.15 and $(x + y)$-values of 0.203 and 0.188 below 0.30, which fully meeting Rec. 2020 standards of (0.131, 0.046) (Fig. 5e), illustrating their great potential as emitters for the high-definition displays.

Discussion

In summary, surface engineering with DBSA ligands significantly enhances the crystal integrity and structural rigidity of $CsPbBr_3$ NPLs, enabling a color-saturated, extremely narrow blue emission with nearly unity absolute PL QY. As determined by DFT calculations and supported by experimental data, covalent bonds are formed between the surface Pb^{2+} cations and DBSA with a binding energy of 5.16 eV, which is much higher than the energy of the ionic bonds between OLA-Br and Pb^{2+} (1.21 eV). The interaction between DBSA and perovskite NPL results in an ordered and stable perovskite surface, and thus yields $CsPbBr_3$ NPLs with uniform shapes and morphology. Moreover, the covalent bonding with DBSA inhibits the phase transition and decomposition of perovskite phase, enabling $CsPbBr_3$ NPLs with excellent structural and optical stability. The PL bandwidth of the color-saturated blue emission of the DBSA-$CsPbBr_3$ NPLs measured at 80 K peaks at 457 nm and reaches an extremely narrow value of 3.7 nm. In comparison with other blue perovskite LEDs, the LEDs based on DBSA-$CsPbBr_3$ NPLs show the narrowest EL bandwidth of 15 nm which corresponds to CIE coordinates of (0.141, 0.062), indicating their significant potential as emitters for ultra-high-definition displays meeting Rec. 2020 standards. DBSA-$CsPbBr_3$ NPLs have demonstrated significantly improved optical performance and stability, which brings blue emitting perovskites closer to commercialization. The DBSA-assisted perovskite nanomaterials can thus be applied in a variety of applications requiring excellent optical performance, including lighting, signaling, and optical communications.

Materials and methods

Materials

Cesium bromide (CsBr, 99.999%), lead bromide ($PbBr_2$, 99.999%), oleic acid (OA, 90%), dimethyl sulfoxide (DMSO, 99.5%), chlorobenzene (CB, 99.5%), and polyethyleneimine (PEI) were obtained from Sigma-Aldrich. Oleylamine (OLA, 80-90%), methyl acetate (99%), and N-butanol (99.8%) were obtained from Aladdin. Hydrobromic acid (40 wt% in H_2O) was purchased from Tianjin Chemical Industry. 4-Dodecylbenzene sulfonic acid (DBSA, 95%) was purchased from Shanghai Acmec Biochemical Co., Ltd. Poly(3,4-ethylenedioxythiophene) polystyrene sulfonate (PEDOT:PSS), poly(4-butylphenyl-diphenyl-amine) (Poly-TPD), 1,3,5-tris(1-phenyl-1H-benzimidazol-2-yl)benzene (TPBi), and 2,4,6-Tris[3-(diphenylphosphinyl)phenyl]-1,3,5-triazine (POT2T) were purchased from Xi'an Polymer Light Technology Corp. Hexane, ethanol, dichloromethane, isopropyl alcohol, toluene, and acetone were obtained from Sinopharm Chemical Reagent Co., Ltd.

Synthesis of $CsPbBr_3$ and DBSA-$CsPbBr_3$ NPLs

The syntheses were conducted under open-air conditions, following the LARP approach. In the first step, 0.1 mmol CsBr was dissolved in 1 mL of 40% HBr, and

1 mmol $PbBr_2$ was dissolved in 2 mL DMSO. To produce $CsPbBr_3$ NPLs, 100 μL $PbBr_2$ precursor was rapidly injected into a 6 mL solution which contained 0.5 mL OA, 0.5 mL OLA, and 5 mL toluene, under continuous stirring. Then, 0.1 mL CsBr precursor was rapidly injected, and after appearance of a turbid white substance, 0.4 mL N-butanol was introduced. Subsequently, centrifugation at 8000 rpm was immediately performed and the supernatant containing $CsPbBr_3$ NPLs was collected. After annealing the supernatant at 65 °C for 1 min, 2-fold volume excess of methyl acetate was added for purification under centrifugation at 10,000 rpm for 5 min. Finally, the precipitate was collected and redispersed in 1 mL toluene. For the synthesis of DBSA-$CsPbBr_3$ NPLs, 100 mg of DBSA ligand was introduced into the mixture of 0.5 mL OA, 0.5 mL OLA, and 5 mL toluene, before injection of the $PbBr_2$ precursor. Other steps were the same as described above.

LED fabrication

Glass substrates with patterned ITO-coating were ultrasonically washed in sequence with deionized water, ethanol, dichloromethane, and isopropyl alcohol for 20 min, and then further cleaned with an oxygen-plasma for 15 min. A PEDOT:PSS solution was spin-coated onto ITO substrates at 4000 rpm for 40 s, followed by annealing at 150 °C for 15 min in ambient conditions. The substrate was transferred into a N_2-filled glovebox, and poly-TPD solution (5 mg mL^{-1}, CB) was spin-coated on top of PEDOT:PSS at 4000 rpm for 40 s, followed by annealing at 150 °C for 15 min. Subsequently, PEI solution (0.15 mg mL^{-1} in isopropyl alcohol) was spin-coated onto the poly-TPD layer at 2000 rpm for 40 s. A 12 nm NPL film (consisting of either $CsPbBr_3$ or DBSA-$CsPbBr_3$ NPLs) was deposited on PEI by spin-coating the NPL solution at 2000 rpm for 40 s. Finally, 5 nm TPBi, 35 nm POT2T, and 100 nm Al films were deposited by thermal evaporation in a vacuum deposition chamber ($\sim 5 \times 10^{-4}$ Pa pressure). A luminous area of 0.04 cm^2 was defined as the overlap between ITO and Al electrodes.

Characterization

FTIR spectra were taken on an IFS-66V/S FTIR spectrophotometer. TEM and HRTEM images were obtained measured on a JEM-2100F transmission electron microscope. XPS measurements were performed on an ESCALAB250 spectrometer. UV-vis absorption spectra were measured on a UV-2600 (Shimadzu) spectrophotometer, and PL spectra on a FLS920P fluorescence spectrometer. Absolute PL QYs were measured on an Edinburgh FLS820-s spectrometer with a calibrated integrated sphere. 1H NMR spectra were obtained at room temperature on a Zhongke Niujin AS400 (400 MHz, 1H) instrument. TRPL measurements were conducted on a time-dependent single photon counting system based on the FLS920P Edinburgh spectrometer with an excitation wavelength of 365 nm. TA spectra were measured using a femtosecond transient absorption pump-probe spectrometer (Ultrafast Systems LLC) with a pump wavelength of 365 nm. XRD patterns were obtained on a Bruker D8 Advance X diffractometer with Cu K_α Source ($\lambda = 1.5406$ Å). SEM images were collected on a Hitachi SU8000 SEM (Hitachi Limited, Tokyo, Japan) under 5 kV acceleration voltage. UPS measurements were performed on a PREVAC system. LED performance was evaluated using the commercially available system (SHENZHEN PYNECT SCIENCE AND TECHNOLOGY Co, Ltd.), with current density-voltage characteristics been recorded on a Keithley 2400 source meter, and light-output measurements on a fiber integration sphere coupled with a QE Pro spectrometer.

Computational methods

The density functional theory (DFT) method as implemented in the Vienna ab initio simulation package (VASP)[67] was adopted. Electron–ion interactions were described using projector-augmented wave pseudopotentials[68]. The generalized gradient approximation[69] of the Perdew, Burke, and Ernzernhof functional (PBE)[70] was employed. A plane-wave kinetic-energy cutoff of 600 eV and a *k*-spacing of 0.18 $Å^{-1}$ in reciprocal space were adopted to achieve reliable results. The Van der Waals (vdW) interaction was considered by adopting optB86b-vdW functional[71], which has been used in similar systems in previous studies[72]. The dipole correction was involved to cancel the artificial field between spurious images due to periodic boundary conditions. All atomistic structures were visualized using VESTA software[73]. The adsorption energy (E_{ad}) was calculated using the following formula[74]: $E_{ad} = E_{ad\_model} - E_{separate\_model}$, where E_{ad_model} is the total energy of the adsorption model, and $E_{separate\_model}$ is the total energy of the model where substrate and ligand were separated by the vacuum with a thickness of 15 Å to eliminate the interaction between them.

Date availability

The data that support the plots within this paper and the other findings of this study are available from the corresponding authors upon reasonable request.

Acknowledgements

The authors acknowledge financial support from the National Key Research and Development Program of China (2022YFE0200200), National Natural Science Foundation of China (52072141, 51972136, 52102170), Postdoctoral Science Foundation of China (2021T140251), and the Innovation and Technology Commission of Hong Kong SAR (MHP/068/21). The grazing-incidence wide-angle X-ray scattering (GIWAXS) data were obtained at beamline BL17B1 of the Shanghai Synchrotron Radiation Facility (SSRF), P.R. China. The grazing incidence X-ray diffraction (GIXRD) experiments were

carried out at beamline 02U2, Shanghai Synchrotron Radiation Facility (SSRF), P.R. China.

Author details
[1]Key Laboratory of Automobile Materials MOE, School of Materials Science & Engineering, and Jilin Provincial International Cooperation Key Laboratory of High-Efficiency Clean Energy Materials, Jilin University, Changchun, China. [2]State Key Laboratory of Supramolecular Structure and Materials, College of Chemistry, Jilin University, Changchun, China. [3]State Key Laboratory of Materials Processing and Die & Mould Technology, School of Materials Science and Engineering, Huazhong University of Science and Technology, Wuhan, Hubei, China. [4]Department of Chemistry, University of Victoria, Victoria, BC, Canada. [5]Key Laboratory of Advanced Display and System Applications of Ministry of Education, Shanghai University, Shanghai, China. [6]Department of Materials Science and Engineering, and Centre for Functional Photonics (CFP), City University of Hong Kong, Hong Kong S.A.R, China

Author contributions
Q.H. and W.Y. performed the material synthesis and fabrication of LEDs, and wrote the draft. B.G. performed theoretical calculations, while Q.Z., D.Y., H.Z. and X.Y. assisted in data collection and analysis. W.Z., X.Z. and A.L.R. designed the experiments; A.L.R. completed revision of the manuscript. All authors contributed to analysis and discussions of the experimental results, and to writing of the manuscript.

Conflict of interest
The authors declare no competing interests.

Supplementary information The online version contains supplementary material available at https://doi.org/10.1038/s41377-024-01441-1.

Received: 13 December 2023 Revised: 27 March 2024 Accepted: 29 March 2024
Published online: 11 May 2024

References

1. Karlsson, M. et al. Mixed halide perovskites for spectrally stable and high-efficiency blue light-emitting diodes. *Nat. Commun.* **12**, 361 (2021).
2. Zhao, M., Zhang, Q. Y. & Xia, Z. G. Narrow-band emitters in LED backlights for liquid-crystal displays. *Mater. Today* **40**, 246–265 (2020).
3. Kovalenko, M. V., Protesescu, L. & Bodnarchuk, M. I. Properties and potential optoelectronic applications of lead halide perovskite nanocrystals. *Science* **358**, 745–750 (2017).
4. Kim, Y. H. et al. Comprehensive defect suppression in perovskite nanocrystals for high-efficiency light-emitting diodes. *Nat. Photonics* **15**, 148–155 (2021).
5. Bai, W. H. et al. Perovskite light-emitting diodes with an external quantum efficiency exceeding 30%. *Adv. Mater.* **35**, 2302283 (2023).
6. Zhang, J. B. et al. Ligand-induced cation-π interactions enable high-efficiency, bright, and spectrally stable Rec. 2020 pure-red perovskite light-emitting diodes. *Adv. Mater.* **35**, 2303938 (2023).
7. Zhang, J. B. et al. A multifunctional "halide-equivalent" anion enabling efficient $CsPb(Br/I)_3$ nanocrystals pure-red light-emitting diodes with external quantum efficiency exceeding 23%. *Adv. Mater.* **35**, 2209002 (2023).
8. Han, T. H. et al. A roadmap for the commercialization of perovskite light emitters. *Nat. Rev. Mater.* **7**, 757–777 (2022).
9. Knight, A. J. & Herz, L. M. Preventing phase segregation in mixed-halide perovskites: a perspective. *Energy Environ. Sci.* **13**, 2024–2046 (2020).
10. Gao, L. et al. High efficiency pure blue perovskite quantum dot light-emitting diodes based on formamidinium manipulating carrier dynamics and electron state filling. *Light Sci. Appl.* **11**, 346 (2022).
11. Liu, H. et al. Organic semiconducting ligands passivated $CsPbBr_3$ nanoplatelets for blue light-emitting diodes. *ACS Energy Lett.* **8**, 4259–4266 (2023).
12. Cao, J. J. et al. Cryogenic-temperature thermodynamically suppressed and strongly confined $CsPbBr_3$ quantum dots for deeply blue light-emitting diodes. *Adv. Opt. Mater.* **9**, 2100300 (2021).
13. Bi, C. H. et al. Suppressing auger recombination of perovskite quantum dots for efficient pure-blue-light-emitting diodes. *ACS Energy Lett.* **8**, 731–739 (2023).
14. Liu, A. Q. et al. High color-purity and efficient pure-blue perovskite light-emitting diodes based on strongly confined monodispersed quantum dots. *Nano Lett.* **23**, 2405–2411 (2023).
15. Yang, D. D. et al. $CsPbBr_3$ quantum dots 2.0: benzenesulfonic acid equivalent ligand awakens complete purification. *Adv. Mater.* **31**, 1900767 (2019).
16. Hassan, Y. et al. Ligand-engineered bandgap stability in mixed-halide perovskite LEDs. *Nature* **591**, 72–77 (2021).
17. Liu, Y. et al. Ligands for $CsPbBr_3$ perovskite quantum dots: the stronger the better? *Chem. Eng. J.* **453**, 139904 (2023).
18. Yang, D. D. et al. Armor-like passivated $CsPbBr_3$ quantum dots: boosted stability with hand-in-hand ligands and enhanced performance of nuclear batteries. *J. Mater. Chem. A* **9**, 8772–8781 (2021).
19. Liu, H. et al. Efficient and stable blue light emitting diodes based on $CsPbBr_3$ nanoplatelets with surface passivation by a multifunctional organic sulfate. *Adv. Energy Mater.* **13**, 2201605 (2023).
20. Wang, H. R. et al. Efficient $CsPbBr_3$ nanoplatelet-based blue light-emitting diodes enabled by engineered surface ligands. *ACS Energy Lett.* **7**, 1137–1145 (2022).
21. Jiang, Y. Z. et al. Synthesis-on-substrate of quantum dot solids. *Nature* **612**, 679–684 (2022).
22. Wang, Y. K. et al. Self-assembled monolayer-based blue perovskite LEDs. *Sci. Adv.* **9**, eadh2140 (2023).
23. Yin, W. X. et al. Emitter structure design of near-infrared quantum dot light-emitting devices. *Mater. Today* **67**, 446–467 (2023).
24. Wang, F. et al. Simultaneous phase and size control of upconversion nanocrystals through lanthanide doping. *Nature* **463**, 1061–1065 (2010).
25. Yang, C. C. & Li, S. Size-dependent phase stability of silver nanocrystals. *J. Phys. Chem. C.* **112**, 16400–16404 (2008).
26. Schlag, S. & Eicke, H. F. Size driven phase transition in nanocrystalline $BaTiO_3$. *Solid State Commun.* **91**, 883–887 (1994).
27. Wang, Y. et al. Chemically stable black phase $CsPbI_3$ inorganic perovskites for high-efficiency photovoltaics. *Adv. Mater.* **32**, 2001025 (2020).
28. Swarnkar, A. et al. Quantum dot-induced phase stabilization of α-$CsPbI_3$ perovskite for high-efficiency photovoltaics. *Science* **354**, 92–95 (2016).
29. Zhang, H. D. et al. Ultra-small-size, highly efficient and stable $CsPbBr_3$ quantum dots synthesized by using a cesium-dodecyl benzene sulfonic acid solution. *Chem. Eng. J.* **473**, 145213 (2023).
30. Vighnesh, K. et al. Hot-injection synthesis protocol for green-emitting cesium lead bromide perovskite nanocrystals. *ACS Nano* **16**, 19618–19625 (2022).
31. Grisorio, R. et al. Insights into the role of the lead/surfactant ratio in the formation and passivation of cesium lead bromide perovskite nanocrystals. *Nanoscale* **12**, 623–637 (2020).
32. Krieg, F. et al. Colloidal $CsPbX_3$ (X=Cl, Br, I) nanocrystals 2.0: Zwitterionic capping ligands for improved durability and stability. *ACS Energy Lett.* **3**, 641–646 (2018).
33. Adhikari, G. C. et al. Synthesis of $CsPbBr_3$ and transformation into Cs_4PbBr_6 crystals for white light emission with high CRI and tunable CCT. *J. Phys. Chem. C.* **123**, 12023–12028 (2019).
34. Thapa, S. et al. Blue-red color-tunable all-inorganic bromide–iodide mixed-halide perovskite nanocrystals using the saponification technique for white-light-emitting diodes. *J. Opt. Soc. Am. B* **36**, 1616–1622 (2019).
35. Zhang, X. Y. et al. Challenges in developing perovskite nanocrystals for commercial applications. *ChemPlusChem* https://doi.org/10.1002/cplu.202300693 (in the press) (2024).
36. Wu, Y. et al. In situ passivation of $PbBr_6^{4-}$ octahedra toward blue luminescent $CsPbBr_3$ nanoplatelets with near 100% absolute quantum yield. *ACS Energy Lett.* **3**, 2030–2037 (2018).
37. Zhang, F. et al. Brightly luminescent and color-tunable colloidal $CH_3NH_3PbX_3$ (X=Br, I, Cl) quantum dots: potential alternatives for display technology. *ACS Nano* **9**, 4533–4542 (2015).
38. Win, A. A. et al. Origin of the near 400 nm absorption and emission band in the synthesis of cesium lead bromide nanostructures: metal halide molecular clusters rather than perovskite magic-sized clusters. *J. Phys. Chem. Lett.* **14**, 116–121 (2023).
39. Zhao, J. Q. et al. Systematic approach of one-dimensional lead perovskites with face-sharing connectivity to realize efficient and tunable broadband light emission. *J. Phys. Chem. C.* **125**, 10850–10859 (2021).
40. Nan, Z. A. et al. Revealing phase evolution mechanism for stabilizing formamidinium-based lead halide perovskites by a key intermediate phase. *Chem* **7**, 2513–2526 (2021).

41. Kong, L. M. et al. Stability of perovskite light-emitting diodes: existing issues and mitigation strategies related to both material and device aspects. *Adv. Mater.* **34**, 2205217 (2022).
42. Huang, H. et al. Control of emission color of high quantum yield $CH_3NH_3PbBr_3$ perovskite quantum dots by precipitation temperature. *Adv. Sci.* **2**, 1500194 (2015).
43. Zhang, X. Y. et al. Water-assisted size and shape control of $CsPbBr_3$ perovskite nanocrystals. *Angew. Chem. Int. Ed.* **57**, 3337–3342 (2018).
44. Espina, A., Sanchez-Cortes, S. & Jurašeková, Z. Vibrational study (Raman, SERS, and IR) of plant gallnut polyphenols related to the fabrication of iron gall inks. *Molecules* **27**, 279 (2022).
45. Wang, Q. et al. Stabilizing the α-phase of $CsPbI_3$ perovskite by sulfobetaine zwitterions in one-step spin-coating films. *Joule* **1**, 371–382 (2017).
46. Sheppard, N. The vibrational spectra of some organic sulphur compounds and the characteristic frequencies of C—S linkages. *Trans. Faraday Soc.* **46**, 429–439 (1950).
47. Yang, D. D. et al. Facet-induced coordination competition for highly ordered $CsPbBr_3$ nanoplatelets with strong polarized emission. *Nano Res.* **15**, 502–509 (2022).
48. Yassitepe, E. et al. Amine-free synthesis of cesium lead halide perovskite quantum dots for efficient light-emitting diodes. *Adv. Funct. Mater.* **26**, 8757–8763 (2016).
49. Yin, W. X. et al. Overcoming the ambient manufacturability-performance bottleneck in perovskite nanocrystal emitters for efficient light-emitting diodes. *Angew. Chem. Int. Ed.* **62**, e202303462 (2023).
50. Lin, H. et al. Stable and efficient blue-emitting $CsPbBr_3$ nanoplatelets with potassium bromide surface passivation. *Small* **17**, 2101359 (2021).
51. Tsai, K. R., Harris, P. M. & Lassettre, E. N. The crystal structure of cesium monoxide. *J. Phys. Chem.* **60**, 338–344 (1956).
52. Duan, Y. Y. et al. Meeting high stability and efficiency in hybrid light-emitting diodes based on SiO_2/ZrO_2 coated $CsPbBr_3$ perovskite nanocrystals. *Adv. Funct. Mater.* **30**, 2005401 (2020).
53. Ma, X. M. et al. The stokes shift and exciton fine structure in strongly confined $CsPbBr_3$ perovskite nanoplatelets. *J. Phys. Chem. Lett.* **14**, 6860–6866 (2023).
54. Venkatesan, N. R., Labram, J. G. & Chabinyc, M. L. Charge-carrier dynamics and crystalline texture of layered Ruddlesden–Popper hybrid lead iodide perovskite thin films. *ACS Energy Lett.* **3**, 380–386 (2018).
55. Rossi, D. et al. Light-induced activation of forbidden exciton transition in strongly confined perovskite quantum dots. *ACS Nano* **12**, 12436–12443 (2018).
56. He, S. et al. Visible-to-ultraviolet upconversion efficiency above 10% sensitized by quantum-confined perovskite nanocrystals. *J. Phys. Chem. Lett.* **10**, 5036–5040 (2019).
57. Guo, Y. S. et al. Dynamic emission stokes shift and liquid-like dielectric solvation of band edge carriers in lead-halide perovskites. *Nat. Commun.* **10**, 1175 (2019).
58. Liu, F. et al. Highly luminescent phase-stable $CsPbI_3$ perovskite quantum dots achieving near 100% absolute photoluminescence quantum yield. *ACS Nano* **11**, 10373–10383 (2017).
59. Zanatta, A. R., Mulato, M. & Chambouleyron, I. Exponential absorption edge and disorder in column IV amorphous semiconductors. *J. Appl. Phys.* **84**, 5184–5190 (1998).
60. Wright, A. D. et al. Electron-phonon coupling in hybrid lead halide perovskites. *Nat. Commun.* **7**, 11755 (2016).
61. Fang, H. H. et al. Photoexcitation dynamics in solution-processed formamidinium lead iodide perovskite thin films for solar cell applications. *Light Sci. Appl.* **5**, e16056 (2016).
62. Zhang, Y. W. et al. Amplified spontaneous emission of perovskite in water: towards under-water lasing. *Mater. Today Phys.* **24**, 100686 (2022).
63. Lin, R. C. et al. All-Inorganic $CsCu_2I_3$ single crystal with high-PLQY (≈15.7%) intrinsic white-light emission via strongly localized 1D excitonic recombination. *Adv. Mater.* **31**, 1905079 (2019).
64. Lu, P. et al. Enrichment of anchoring sites by introducing supramolecular halogen bonds for the efficient perovskite nanocrystal LEDs. *Light Sci. Appl.* **12**, 215 (2023).
65. Zhang, B. B. et al. Electron-phonon coupling suppression by enhanced lattice rigidity in 2D perovskite single crystals for high-performance X-Ray detection. *Adv. Mater.* **35**, 2208875 (2023).
66. Huang, Y. M. et al. A-site cation engineering for highly efficient $MAPbI_3$ single-crystal X-ray detector. *Angew. Chem. Int. Ed.* **58**, 17834–17842 (2019).
67. Kresse, G. & Joubert, D. From ultrasoft pseudopotentials to the projector augmented-wave method. *Phys. Rev. B* **59**, 1758–1775 (1999).
68. Blöchl, P. E. Projector augmented-wave method. *Phys. Rev. B* **50**, 17953–17979 (1994).
69. Perdew, J. P. & Wang, Y. Accurate and simple analytic representation of the electron-gas correlation energy. *Phys. Rev. B* **45**, 13244–13249 (1992).
70. Perdew, J. P., Burke, K. & Ernzerhof, M. Generalized gradient approximation made simple. *Phys. Rev. Lett.* **77**, 3865–3868 (1996).
71. Klimes, J., Bowler, D. R. & Michaelides, A. Chemical accuracy for the van der Waals density functional. *J. Phys.: Condens. Matter.* **22**, 022201 (2010).
72. Zhang, S. et al. Minimizing buried interfacial defects for efficient inverted perovskite solar cells. *Science* **380**, 404–409 (2023).
73. Momma, K. & Izumi, F. *VESTA*: a three-dimensional visualization system for electronic and structural analysis. *J. Appl. Crystallogr.* **41**, 653–658 (2008).
74. Dong, J. C. et al. Deep-blue electroluminescence of perovskites with reduced dimensionality achieved by manipulating adsorption-energy differences. *Angew. Chem. Int. Ed.* **61**, e202210322 (2022).
75. Chen, F. et al. Bilayer phosphine oxide modification toward efficient and large-area pure-blue perovskite quantum dot light-emitting diodes. *Sci. Bull.* **68**, 2354–2361 (2023).
76. Song, L. et al. Efficient $CsPbBr_3$ sky-blue perovskite light-emitting devices Co-regulated by dual polymer additives. *J. Lumin.* **261**, 119915 (2023).